Highly rarefied gas flows in rough channels of finite length

Zheng Shi[1], Yulong Zhao[2], Wei Su[3,4*] and Lei Wu[1*]

*Correspondence:
weisu@ust.hk; wul@sustech.edu.cn

[1] Department of Mechanics and Aerospace Engineering, Southern University of Science and Technology, Shenzhen 518055, China
[2] State Key Laboratory of Oil and Gas Reservoir Geology and Exploitation, Southwest Petroleum University, Chengdu 610500, China
[3] Division of Emerging Interdisciplinary Areas, The Hong Kong University of Science and Technology, Clear Water Bay, Hong Kong, China
[4] Department of Mathematics, The Hong Kong University of Science and Technology, Clear Water Bay, Hong Kong, China

Abstract

Highly rarefied gas flows through a rough channel of finite length with small bumps appended to its surfaces are investigated, by varying the accommodation coefficient α in Maxwell's diffuse-specular boundary condition, the characteristic size and position of the bumps, and the channel length. First, we study the influence of the surface bumps and consider the rarefied gas flow in a unit channel with periodic boundary conditions to remove the end effect. It is found that the surface bumps have a significant impact on the flow permeability. When α is very small (i.e., nearly specular reflection of gas molecules at the channel surface), the apparent gas permeability is dramatically reduced, even in the presence of small bumps, to a value that is almost comparable to the one when fully diffuse gas-surface scattering is assumed. This impact can be taken into account through an effective accommodation coefficient, i.e., the permeability of the rough channel is taken equivalently as that of a smooth channel without bumps but having gas-surface scattering under the effective accommodation coefficient. Second, we study the end effect by connecting a smooth channel of length L_0 to two huge gas reservoirs. It is found that (i) the end correction length is large at small α. Consequently, the mass flow rate barely reduces with increasing L_0 rather than scales down by a factor of $1/L_0$ as predicted by the classical Knudsen diffusion theory; and (ii) the end correction is related to the channel's aspect ratio. Finally, based on the effective accommodation coefficient and end correction, we explain the exotic flow enhancement in graphene angstrom-scale channels observed by Geim's research group (Keerthi et al, Nature 558:420–424, 2018).

Keywords: Rarefied gas, Accommodation coefficient, Rough channel, End effect

1 Introduction

Permeability is the measure of flow capacity in porous media. It is a key parameter in a number of engineering applications, such as the commercial extraction of shale gas [1] and membrane separation [2]. In shale gas extraction, a considerably large value of permeability indicates exploitable shale gas, while how a system determines the actual fluid permeation and selectivity is essential in realizing practical membrane separation. Conventionally, the permeation of a low-speed flow through a porous medium is described by the Darcy law:

$$\overline{U} = -\frac{k}{\mu L_0} \Delta p, \tag{1}$$

which demonstrates that the discharge per time $\overline{U}$ (in the unit of meter per second) is proportional to the permeability k (in the unit of square meter) and the pressure drop Δp over the porous medium, and inversely proportional to the medium length L_0 and the dynamic viscosity μ of the fluid. The permeability k, usually called intrinsic permeability, is determined by the material and topological structure of the porous medium, and is irrespective of the fluid.

The Darcy law can be derived from the Navier-Stokes equations, for which the primary assumptions are sufficient intermolecular collisions among fluid molecules and non-slip velocity at the solid surface. However, these assumptions can be violated in gas transport with low density and small characteristic flow length, making the gas permeability no longer a constant for a given porous medium. For instance, in shale gas reservoirs, most of the gas is stored and transported in nanoscale matrix pores with diameters of $2 \sim 50$ nm [3–6], where the pore size is in the same order of magnitude as the mean free path of gas molecules so that gas-surface interactions begin to dominate over intermolecular collisions and apparent velocity slip appears at the solid boundary [7–10]. From a systematic experiment, Klinkenberg found that the slippage of gases along pore surfaces gives rise to an enhanced permeability that increases with the reciprocal average gas pressure [11]. To distinguish it from the intrinsic permeability, we call this permeability the apparent gas permeability (AGP) k_a. The enhancement of gas transport is also observed in atomically thin (angstrom-scale) structures such as carbon nanotubes and nano-porous films made from graphene and other two-dimensional (2D) materials [12, 13]. In such structures, the size of a transport channel is much smaller than the molecular mean free path; therefore, gas molecules are most likely to collide with the channel surface rather than each other. The emergence of angstrom-scale systems has offered new opportunities to develop separation membranes with ideal performance, high mechanical strength and chemical resistance [14].

The enhanced AGP is a consequence of gas rarefaction effects, which are related to the Knudsen number Kn, defined as the ratio of the mean free path of gas molecules λ to the characteristic flow length H (i.e., the transverse dimension of the flow channel):

$$Kn = \frac{\lambda}{H} = \frac{\mu(T_0)}{\overline{p}H} \sqrt{\frac{\pi R T_0}{2}}, \tag{2}$$

where $\overline{p}$ is the average gas pressure, T_0 is the gas temperature and R is the gas constant. Based on the value of Kn, gas transport mechanisms are roughly classified into continuum flow ($Kn < 0.001$), slip flow ($0.001 \leq Kn < 0.1$), transition flow ($0.1 \leq Kn < 10$) and free-molecular flow ($Kn \geq 10$). The Darcy law with intrinsic permeability is valid only in the continuum flow. The Navier-Stokes equations equipped with slip-velocity boundary conditions are applicable in the slip flow. Nevertheless, the continuum assumption breaks down in transition and free-molecular flows, so that the Navier-Stokes equations should be replaced by physical laws of gas kinetic theory, such as the Knudsen diffusion theory [15] and the Boltzmann equation [16].

In addition to the Knudsen number, experimental and numerical evidence has demonstrated the vital role of gas-surface interactions in determining the gas transport properties of flows falling into the free-molecular regime [12, 15, 17]. In a recent experiment conducted by Geim's research group, molecular flow rates of helium were measured in angstrom-scale 2D channels made from cleaved crystals such as the graphite, hexagonal boron nitride (hBN) and molybdenum disulfide (MoS_2). It was found that the gas transport rate strongly depends on wall materials [13]: the flow rate through MoS_2 channels can be predicted by the classical Knudsen diffusion theory, which is monotonously reduced as the channel length L_0 increases (with a scaling of $1/L_0$). On the contrary, the flow rate is further enhanced in graphene and hBN channels, which remains constant when the channel length enlarges. These observations were attributed to different materials exhibiting surfaces of different atomic landscapes. The MoS_2 surface with strong corrugations is relatively rough, where helium molecules are more likely to undergo diffuse scattering thus the Knudsen theory works well; however, surfaces of graphene and hBN are much flatter and smoother, from which gas molecules can be specularly reflected with negligible loss of momenta. Besides the length dependence/independence, the magnitude of flow enhancement is also a function of channel height in the three types of channels.

Although surface corrugation and roughness can be used to qualitatively distinguish the different flow enhancements in channels with different materials, it cannot properly describe why the measured flow rate is a function of the channel height. Also, it cannot explain why the flow rate is not a function of the channel length in graphene and hBN channels. In this paper, we aim to quantify the free-molecular flow through rough channels of finite length and offer a comprehensive explanation to Geim's experiment [13]. The analysis is based on the numerical solution of the linearized Bhatnagar-Gross-Krook (BGK) Boltzmann kinetic model equation [18]. Surface corrugation is modeled by small bumps appended to the channel surface, and gas-surface scattering is described by the classical Maxwell's diffuse-specular boundary condition. Thus, the surface roughness is characterized by the bump size and position, as well as the accommodation coefficient in Maxwell's boundary condition. Since the molecular diffusion along the solid surface is negligible [19], we shall focus on the dependence of AGP on the surface corrugation, the accommodation coefficient, and the end effect caused by the finite channel length. We emphasis that although the molecular dynamics simulation can be used to investigate gas transport through nano- and sub-nano-channels [20–22], it is not effective in evaluating the end effect involving large system sizes due to massive computational consumption. Also, it is noted that the thermal effect is negligible in this problem, so the accommodation coefficient can be called tangential momentum accommodation coefficient; although the Maxwell boundary condition is considered, the use of other boundary conditions with a similar value of tangential momentum accommodation coefficient should not alter the major conclusion here.

The rest of this paper is constructed as follows. In Section 2, the linearized BGK model equation and the numerical scheme are briefly described. In Section 3, numerical simulations are performed to analyze how the AGP in a unit channel varies with the Knudsen number, the bump size and position, and the accommodation coefficient. In Section 4, the end effect is investigated by connecting a channel with finite length to two large

gas reservoirs. In Section 5, we provide a reasonable explanation for the observation in Geim's experiment. Conclusions and outlooks are given in Section 6.

2 Gas kinetic theory

As shown in Fig. 1, we consider a 2D pressure-driven gas flow between two parallel plates in a Cartesian coordinate system. The ends of the channel are connected to two large reservoirs containing gas at different pressures. Rectangular bumps, each with height h and width w, are attached to the inner channel surfaces and distributed periodically along the horizontal direction. The adjacent upper and lower bumps are separated by a distance of 2δ. When $\delta = 0$, bumps are symmetrically distributed on the inner surfaces.

We assume that the pressure difference at the two gas reservoirs is small, so that the linearized kinetic equation can be used. This assumption implies that the transport rate of the gas flow would be linearly proportional to the pressure difference, which agrees well with the experimental observations [13]. Since a steady state is of interest, the time-independent linearized BGK-Boltzmann kinetic equation is adopted to describe the rarefied gas dynamics [23]:

$$\boldsymbol{v} \cdot \frac{\partial f}{\partial \boldsymbol{x}} = \frac{\sqrt{\pi}}{2Kn}\left[n + 2\boldsymbol{U} \cdot \boldsymbol{v} + \tau\left(v^2 - 1\right) - f\right], \tag{3}$$

where $f(\boldsymbol{v}, \boldsymbol{x})$ is the perturbed velocity distribution function (i.e., it is the marginal distribution function in which the perturbation of the distribution function is multiplied by $\exp(-v_3^2)/\sqrt{\pi}$ and integrated with respect to the molecular velocity v_3 that is perpendicular to the computational domain) from the equilibrium Maxwell-Boltzmann distribution function $f_{eq} = \exp(-v^2)/\pi$, $\boldsymbol{v} = (v_1, v_2)$ is the molecular velocity normalized by the most probable speed $v_m = \sqrt{2RT_0}$ of gas molecules, and $\boldsymbol{x} = (x_1, x_2)$ is the spatial coordinate normalized by H, with the subscripts "1" and "2" denoting the horizontal and vertical directions, respectively. The perturbed number density n, macroscopic flow velocity $\boldsymbol{U} = (U_1, U_2)$ and perturbed temperature are calculated via the velocity distribution function as

$$n = \iint f f_{eq} dv_1 dv_2, \quad \boldsymbol{U} = \iint \boldsymbol{v} f f_{eq} dv_1 dv_2, \quad \tau = \iint v^2 f f_{eq} dv_1 dv_2 - n, \tag{4}$$

so that Eq. (3) is an integro-differential equation. The temperature of the solid surface is maintained at T_0.

It should be noted that although we are interested in the highly rarefied gas flow, the collision operator in the right hand side of Eq. (3) cannot be dropped. The reasons are, (i) for the Poiseuille flow between parallel plates, the mass flow rate in the free-molecular regime is a logarithmic function of Kn. Therefore, if we drop the collision
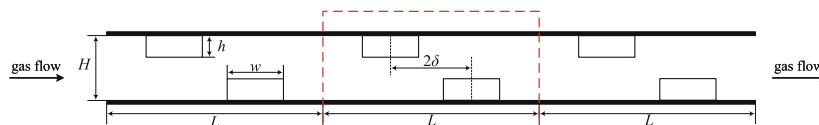

Fig. 1 Schematic of a gas flow through a two-dimensional channel with bumps attached on the inner surfaces. The height and width of the bumps is h and w, respectively, while the bump offset is 2δ. If the channel is sufficiently long, then the gas kinetic theory can be applied only in the unit cell (inside the red box) to save the computational resource

operator, the mass flow rate will be infinite; (ii) in the study of end effect the gas flow is multiscale (e.g., in the reservoir it is in the continuum flow regime, while in the narrow channel it is in the free-molecular flow regime), and the collision operator must be kept. Also note that although the perturbed temperature appears in the collision operator, it does not affect the mass flow rate for the considered flow below.

Although the Boltzmann equation is well validated in describing rarefied gas dynamics, such as normal shock wave and sound wave propagation [24], so far the gas-surface interaction still relies on empirical model and parameters [25]. Here we consider the widely used Maxwell's diffuse-specular boundary condition, where the impinged molecules reflected from the solid wall undergo diffuse and specular reflections, and the ratio of the number of diffuse reflections is quantified by the accommodation coefficient α. Pure diffuse and specular reflections have $\alpha = 1$ and 0, respectively. And the smaller the value of α, the larger the flow rate in the transition flow and free-molecular flow regimes, due to the less loss of momentum. In this linearized problem, Maxwell's diffuse-specular boundary condition at the solid surface reads [26]:

$$f(\boldsymbol{x}, \boldsymbol{v}) = (1 - \alpha)f(\boldsymbol{x}, \boldsymbol{v} - 2\boldsymbol{n}v_n) + \frac{2\alpha}{\sqrt{\pi}} \int_{v'_n < 0} |v'_n| f(\boldsymbol{x}, \boldsymbol{v}') \exp(-v'^2) dv'_1 dv'_2, \qquad (5)$$

where $\boldsymbol{n}$ is the outer normal vector of the solid surface, and v_n is the velocity component in the normal direction.

The kinetic equation is solved by the deterministic discrete velocity method [27], where the molecular velocity space $\boldsymbol{v}$ is represented by a set of discrete velocities. In highly rarefied gas flows, because the bump's corner is convex, the velocity distribution function is discontinuous at the molecular velocity departing from the base surface and traveling in the grazing direction to the bump's corner [28]. Because there are infinitely many bumps, there are so many discontinuities; thus the numerical analysis of Eq. (3) is challenging. This difficulty is overcome by using the non-uniformly refined velocity grid [29]:

$$v_{1,2} = \frac{5}{(N_v - 1)^3}(-N_v + 1, -N_v + 3, \cdots, N_v - 1)^3, \qquad (6)$$

where the discrete velocities are distributed in a square of $[-5, 5]^2$, and are refined near $v_{1,2} = 0$. This type of velocity space discretization has proved to be accurate in simulations of micro-/nano-scale gas flows, especially in capturing the rapid variations in the velocity distribution function at large Knudsen numbers [27]. We take $N_v = 72$, since increasing N_v from 72 to 96 only changes the mass flow rate by about 1.5%.

The spatial region is also divided non-uniformly, with refined grid points near the solid wall. The discretized kinetic equation is solved by the general synthetic iterative scheme [30, 31], where the iteration is terminated when the relative error in the dimensionless mass flow rate:

$$G_p = \int_0^1 U_1(x_2) dx_2 \qquad (7)$$

between two consecutive iteration steps is less than 10^{-5}.

3 Results without the end effect

We first consider the case where the channel is sufficiently long, so that the end effect at the inlet and outlet can be neglected [32, 33]. Under this circumstance, we do not need to simulate the whole channel and reservoirs, but only the unit cell, denoted by the red box, of the size $H \times L$, see Fig. 1. In addition to Maxwell's boundary condition at the solid walls, the following periodic boundary conditions are used on the left and right boundaries of the unit channel [16]:

$$\begin{cases} f(0, x_2, \boldsymbol{v}) = 1 + f\left(\frac{L}{H}, x_2, \boldsymbol{v}\right), & \text{when } v_1 > 0, \\ f\left(\frac{L}{H}, x_2, \boldsymbol{v}\right) = -1 + f(0, x_2, \boldsymbol{v}), & \text{when } v_1 < 0, \end{cases} \tag{8}$$

implying that the flow is driven by the unit pressure gradient pointed to the negative direction of x_1. The AGP, which is normalized by H^2, is calculated as

$$k_a = \frac{2Kn}{\sqrt{\pi}} G_P. \tag{9}$$

We consider the rarefied gas flow in the free-molecular flow regime as relevant to the experiment [13]. In this case, for the flow through two parallel, infinite, and smooth (i.e., without small bumps) plates, it is well known that the dimensional mass flow rate is a logarithmic function of the Knudsen number, while for the flow through a smooth channel with a two-dimensional cross-section, the mass flow rate approaches a constant [34]. Figure 2 shows that, even in the presence of bumps of a size $h \times w = 0.1H \times 0.2H$, the flow rate increases logarithmically with Kn. Without loss of generality, we can consider the representative case of $Kn = 10$ in the following paper.

It is well known that, for a smooth channel without bumps, the mass flow rate is a function of the accommodation coefficient, which is roughly proportional to $(2 - \alpha)/\alpha$. For instance, when $\alpha = 0.1$ and 0.01, the mass flow rate at $Kn = 10$ is 10.5 and 90.9, which are larger than 1.04 under the fully diffuse gas-surface scattering by one and two orders of magnitude, respectively. Therefore, the flow rate of rarefied gas flow through channels with near-specular-reflection surfaces (i.e., the accommodation coefficient is close to zero) is much larger than that through channels with diffusive surfaces. However, when the bumps are added to the surfaces of a smooth channel, the mass flow rate under a small accommodation coefficient of $\alpha = 0.01$ is dramatically reduced, to a value that is almost comparable to that of the smooth channel with $\alpha = 0.5$, see Fig. 2. A similar behavior is also observed in the hypersonic flow in the slip flow regime [35]. In this section, we try to pinpoint the major factors that cause this huge reduction.

3.1 Bump height

We fix the bump width, and the bump offset at $\delta = 0$, but vary the bump height to systematically investigate its influence on the flow velocity and the AGP. The unit cell (red box in Fig. 1) considered has a size of $H \times H$.
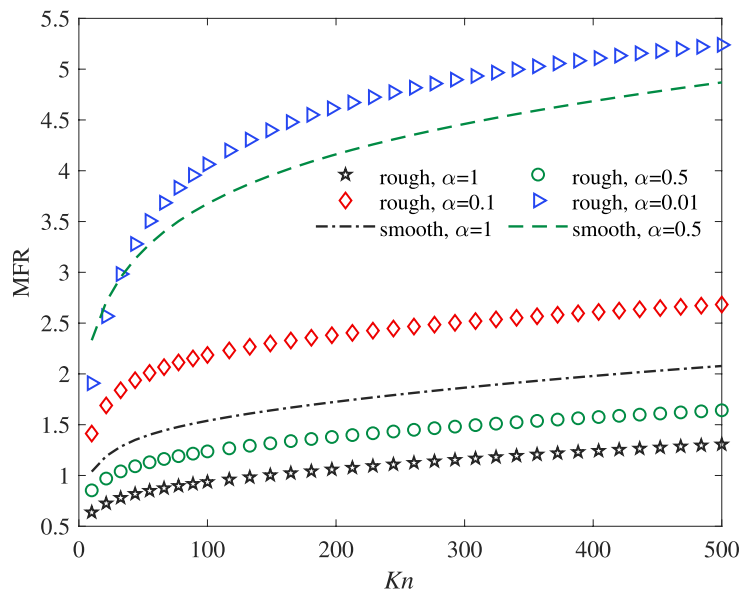
Fig. 2 The dimensionless mass flow rate as a function of the Knudsen number, with different values of accommodation coefficient. The size of the unit channel is $H \times H$. In the rough channel, each bump has a size of $h \times w = 0.1H \times 0.2H$, and the offset distance is $\delta = 0$

Figure 3 depicts the streamlines and the magnitude of flow velocity in the bottom half unit cell, when the accommodation coefficient is $\alpha = 0.01$. The bumps directly disturb the velocity profile, where the corner hinders the gas flow's capability to approach the wall, resulting in significant energy loss and reduction of boundary velocity slip. With the increase of bump height, the size of vortices near the corner increases. The region in which the flow velocity is close to zero begins to extend to
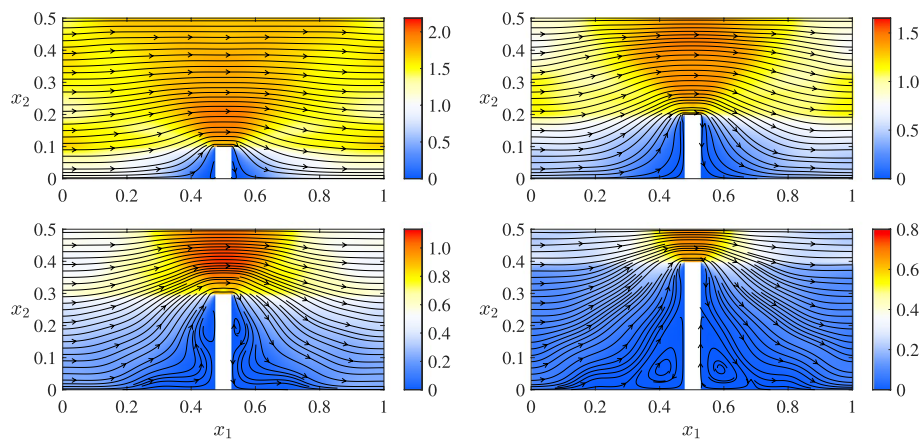

Fig. 3 Streamlines and magnitude of velocity in lower half of the unit channel having a size of $H \times H$, when accommodation coefficient $\alpha = 0.01$ and $w = 0.05H$. The bump heights are $h = 0.1H$, $0.2H$, $0.3H$, and $0.4H$, respectively

both ends of the unit channel. The mass flow rate is greatly reduced, not only because the effective channel height is smaller, but also because the peak flow speed drops. The streamlines and velocity magnitude for other values of accommodation coefficient are more or less the same (not shown).

Figure 4 shows the velocity distribution in the x_1 direction at the inlet and horizontal middle of the channel, when $\alpha = 1$ and $\alpha = 0.01$. When the fully diffuse boundary condition is considered, we see that the flow's horizontal velocity gradually increases from the solid surface to the channel center, and the maximum horizontal speed appears in the channel center ($x_2 = 0.5H$). However, when the near-specular boundary condition (e.g., $\alpha = 0.01$) is considered, the horizontal speed at the channel inlet does not monotonically increase from the channel surface to the center, but has several peaks. Moreover, at $x_1 = 0.5H$, the maximum horizontal speed does not appear at the channel center ($x_2 = 0.5H$), but at the top surface of the bump, i.e., the velocity profile is inverted, which is contrast to the conventional pressure-driven flow.

When the bump height increases, it is seen from Fig. 4 that the velocity slip near the wall decreases. Near the solid surface, as the height of the bump increases, the frequency of collisions between the gas molecules and the wall also increases, leading to a more significant energy loss and a decrease in velocity near the wall. At the same height as the bump ($x_2 = h$), in channels with near-specular reflecting walls, the velocity reaches the peak.

Figure 5 shows the effect of bump height on the AGP at different accommodation coefficients. It is seen that, when α is fixed, when the bump height is very small, the change of bump height has almost no effect on the AGP. As the bump height gradually increases, the smaller the value of α, the more sensitive of the AGP to the change of bump height. When the bump height increases to a certain extent, the AGP decreases dramatically with the increase of bump height. In fact, when the bump height approaches 0.5, the permeability is dominated by this small channel (formed by bumps) of effective height $H - 2h$. Since in the straight channel the permeability is proportional to the height square, we see in the inset of Fig. 5 that the AGP is approximately a quadratic function of $\tilde{h} = 0.5H - h$.
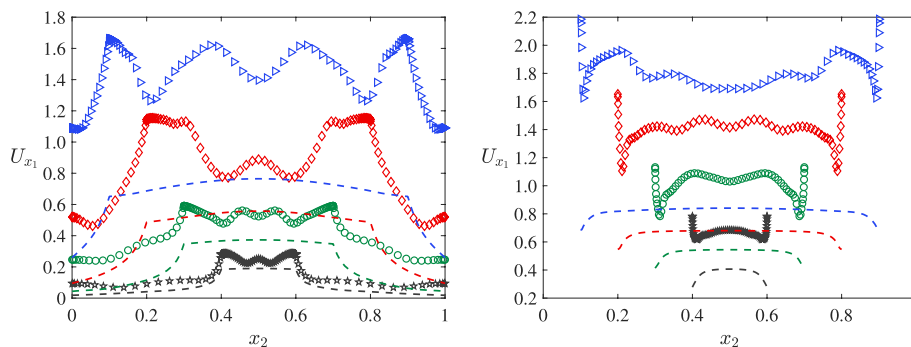

Fig. 4 Horizontal velocity profiles for different values of bump height, when the bump width is $w = 0.05H$. (Left) at inlet: $x_1 = 0$. (Right) at the middle of channel: $x_1 = 0.5H$. Symbols: $\alpha = 0.01$. Lines: $\alpha = 1$. In each figure, in each group of line styles, from top to bottom, the bump height is $h = 0.1H$, $0.2H$, $0.3H$, and $0.4H$, respectively
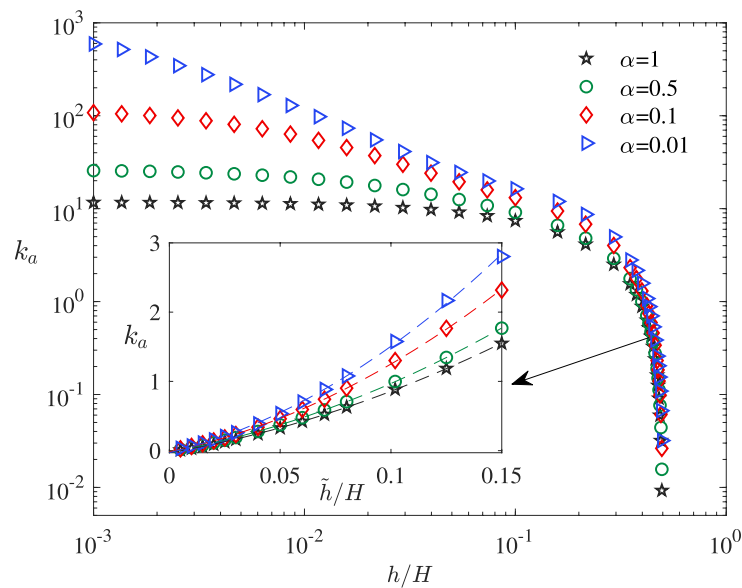
Fig. 5 The AGP as a function of the bump height. The unit channel size is $H \times H$. The bump width is fixed to be $0.2H$, and the offset distance $\delta = 0$. Note that in the inset, $\tilde{h} = 0.5H - h$

3.2 Bump width

To investigate the effects of bump width on the AGP, the height of bumps is fixed at $h = 0.1H$ and $0.01H$, respectively, and the accommodation coefficient is chosen to be 0.01. The numerical results are visualized in Fig. 6a. When $w = 0$, there are no bumps, the inner surface of the channel is completely smooth, and the AGP is large due to the large proportion of specular reflection at the solid surface. When the bump width increases only a little bit, so that the bumps look like thin plates, the AGP drops dramatically: the higher the bump, the larger the drop. Then, the AGP remains nearly unchanged when the bump width gradually increases up to $w = 0.8H$. When the bump width gradually approaches the whole channel length $w = H$, we see a rapid surge in the AGP. This is because now the distance between the bumps is very narrow and the channel can be viewed as a smooth channel again. In the limit of $w = H$, the AGP is slightly smaller than that of $w = 0$, because the effective channel height is now reduced from H to $H - 2h$. This example shows that the bump height plays a significant role in the AGP reduction, rather than the bump width.

3.3 Bump offset distance

Since the distribution of rough elements is random in the realistic scene (e.g., when the channel adsorbs some impurities, such as the PMMA polymer molecules on the graphene surface [13]), a single simplified model may not be accurate enough in describing the gas flow through a real rough channel. However, it can be seen from Fig. 6b that, changes in bump distribution, through adjusting the offset distance δ, do not significantly affect the AGP. For example, the variation of AGP with respect to δ increases when the accommodation coefficient decreases, but even when $\alpha = 0.01$ the highest to the lowest AGP is only about 1.3 over the whole range of bump offset.
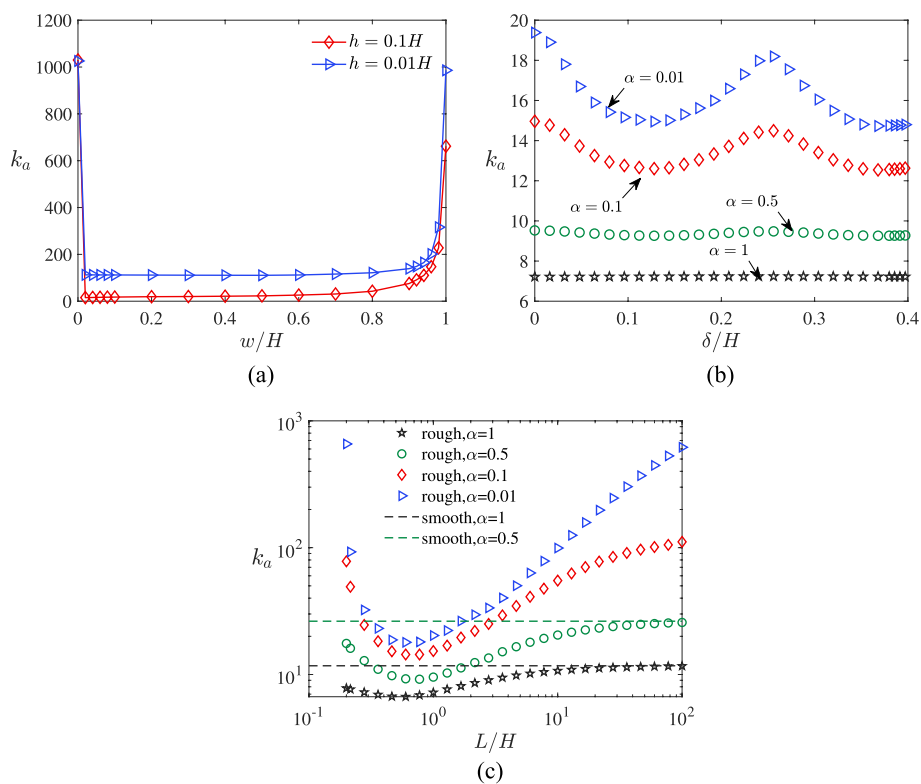
Fig. 6 **a** The AGP as a function of the bump width. The offset distance is $\delta = 0$, and the accommodation coefficient is $\alpha = 0.01$. **b** The AGP as a function of the offset distance δ. The bump size is $0.1H \times 0.2H$. In both figures, the unit channel size is $H \times H$. **c** The AGP as a function of the channel length. The bump size is $0.1H \times 0.2H$, and the offset distance is $\delta = 0$

3.4 Unit channel length

Now we fix the channel height, bump size and position, but increase the unit channel length L to see its effect on the AGP. The value of L represents the spacing among the repeated bumps in the full channel. As shown in Fig. 6c, when the channel length is infinitely close to the bump width, the channel is equivalent to a smooth channel, which causes a high AGP. As the unit channel length increases, the channel surface becomes rough and the obstruction to the gas flow increases, so the AGP decreases gradually. Note that there is still a sudden drop in the initial process of increasing the channel length from $L = 0.2H$, the reason of which is explained in Section 3.2. The minimum AGP occurs at $L/H \approx 0.6$. When the channel length increases to a certain degree, the flow space of the channel becomes larger and larger, which leads to an increase in the AGP. Finally, with the continuous increase of the channel length, the AGP tends to saturate. The position where the AGP tends to saturate increases with the decreasing of accommodation coefficient. For example, when $\alpha = 1$ and 0.1, the location occurs at $L/H = 60$ and $L/H = 100$, respectively.

3.5 Effective accommodation coefficient

The reduction of AGP at a small value of accommodation coefficient in the rough channel with surface bumps can be reflected through an effective accommodation coefficient,

where the flow capacity of the rough channel is equivalent to that through a smooth channel without bumps but having gas-surface scattering under the effective accommodation coefficient $\alpha_{\text{effective}}$. Since the AGP is not sensitive to the width and offset distance of bumps, here we investigate the effective accommodation coefficient of the rough channel by fixing the bump width at $w = 0.2H$ and offset distance at $\delta = 0$. We still consider the unit channel of size $H \times H$, see the red box in Fig. 1. The effective accommodation coefficient is determined in the following manner. First, we choose $\alpha = 1$, and calculate the AGP of a rough channel at $Kn = 10$. Then, we choose a smooth channel with $\alpha = 1$, and adjust the channel height to make its AGP equal to that of the rough channel. Finally, we get the AGP of the rough and smooth channels at different values of accommodation coefficient; by equating the AGP of the rough channel to that of the smooth channel, we determine $\alpha_{\text{effective}}$ of the rough channel to be that of the smooth channel (see the points of intersection between the dashed lines and solid lines in Fig. 7). For example, in Fig. 7 we see that, when $\alpha = 1$, the AGP of the rough channel with bump size $h \times w = 0.1H \times 0.2H$ is the same as that of the smooth channel with a height of $0.766H$. When the accommodation coefficient of this rough channel is less than 0.001, the effective accommodation coefficient of this channel is about 0.404. Similarly, when the rough channel has bump heights of $0.2H$, $0.3H$, and $0.4H$, the effective channel height of the smooth channel is $0.578H$, $0.400H$, and $0.218H$, while $\alpha_{\text{effective}}$ of the rough channel (when the true accommodation coefficient is very small) is 0.451, 0.468, and 0.491, respectively. Thus, a small bump results in a huge reduction of permeability, or equivalently, a large increase of the effective accommodation coefficient.

When w/H is not close to 1, in the limit of $h \to 0$, and the true accommodation coefficient approaches zero, the effective accommodation coefficient, as obtained in the numerical simulation, can be approximately given by
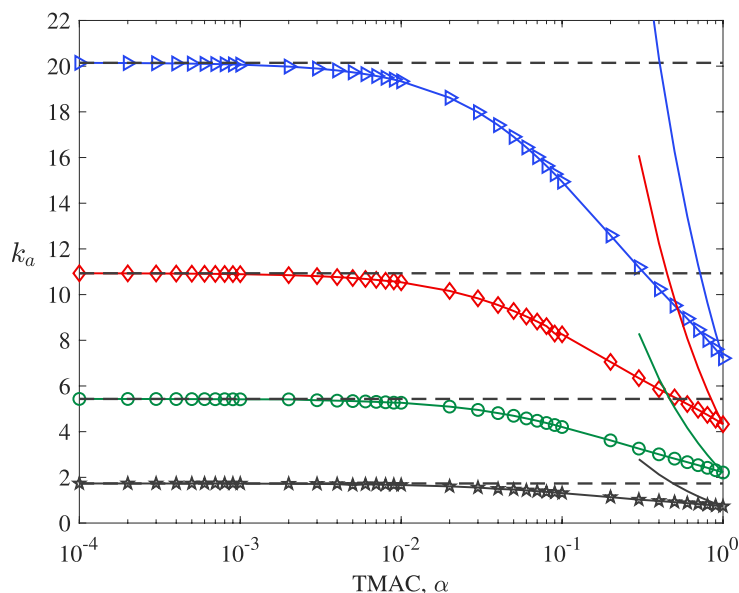

Fig. 7 The effective accommodation coefficient, when the unit channel size is $H \times H$. In each group of line styles, from top to bottom, the bump height is $h = 0.1H$, $0.2H$, $0.3H$, and $0.4H$, respectively. The solid lines, from top to bottom, show the AGP of the smooth channel with heights of $0.766H$, $0.578H$, $0.400H$, and $0.218H$, respectively. The bump width is fixed at $w = 0.2H$

$$\alpha_{\text{effective}} \approx 10\frac{h}{H}, \tag{10}$$

while the enhancement ratio K, i.e., the permeability normalized by the permeability obtained from the diffuse scattering, is

$$K \approx \frac{1}{\alpha_{\text{effective}}} \approx 0.1\frac{H}{h}. \tag{11}$$

When w/H is close to 1, the result in Fig. 8 shows that $\alpha_{\text{effective}}$ is not significantly larger than the true accommodation coefficient. For example, when $w/H = 0.95$, $\alpha_{\text{effective}}$ is only about 5 times larger than α.

4 End effect

In the previous section, we considered gas flows between two parallel and infinitely long plates, where the end effect (i.e., pressure loss at the inlet and outlet of a finite channel) is neglected. Nevertheless, in an experiment, flow rates are usually measured through channels of finite lengths, where the ends of a channel are connected to two large reservoirs maintained at different conditions (e.g., containing gases with different pressures to drive the flow by pressure gradient). The influence of the inlet and outlet ends contributes to the length dependence of the flow rate. Based on the concept of effective channel length, end corrections for flow rates of rarefied gases through moderate long tubes were developed under the assumption of fully diffuse gas-surface scattering [32, 33]. In this section, we investigate the end effect when pure diffuse scattering breaks down.

The schematic diagram of the computational domain is illustrated in Fig. 9. A 2D channel having a size of $L_0 \times H$ is connected to two large reservoirs that are filled
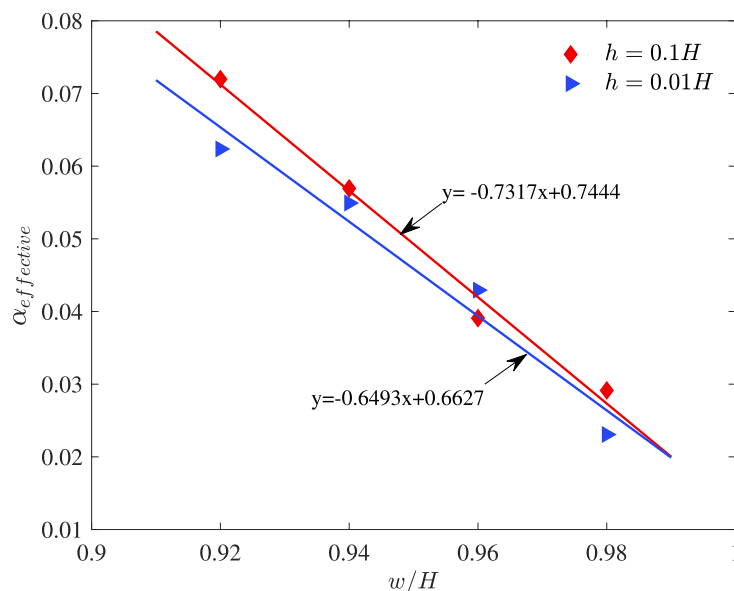

Fig. 8 The effective accommodation coefficient as a function of the bump width, when the unit channel size is $H \times H$, the offset distance is $\delta = 0$, and the accommodation coefficient is $\alpha = 0.01$. Symbols represent the numerical results, while solid lines are the linear fitting curves to guide the eye
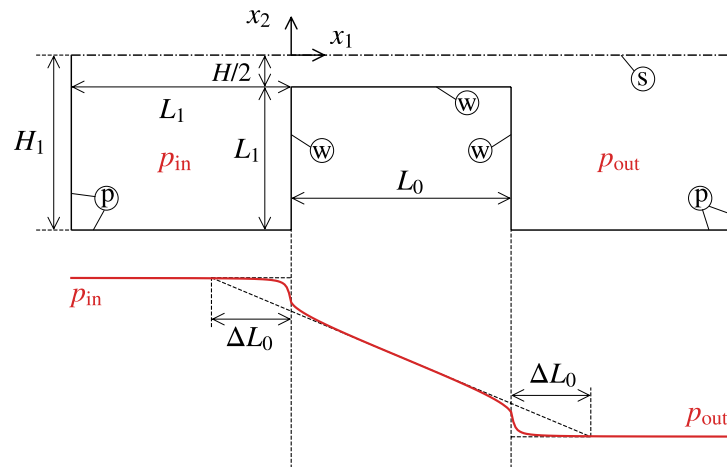
Fig. 9 Schematic of the computational domain and pressure distribution to quantify the end effect. A 2D channel with a size of $L_0 \times H$ is connected to two large reservoirs filled with gas maintained at pressures p_{in} and p_{out}, respectively. The flow field is simulated on the lower half of the geometry due to symmetry. No bumps are appended to channel surfaces. The distribution of gas pressure along the horizontal center line (dash-dotted line) for $\alpha = 0.1$ is shown in solid red line. End effect causes pressure jump at the inlet/outlet of the channel and can be taken into account by the increment ΔL_0 to the channel length [33]

with gas maintained at pressures of p_{in} and p_{out} with $p_{in} > p_{out}$, respectively. Consequently, the gas is driven from the left reservoir to the right one. The origin of the horizontal axis x_1 is fixed at the center of the inlet cross section of the channel. An expected pressure distribution along the horizontal center line (dash-dotted line) is also plotted. It shows that the gas pressure varies linearly inside the channel at locations far from its inlet and outlet ends; but the linear dependence changes in the areas around the inlet and outlet of the channel and the pressure eventually approaches the values in the reservoirs. The end effect causes a pressure jump at the inlet (outlet) cross section, i.e., $x_1 = 0$ ($x_1 = L_0/H$), where the pressure is not equal to p_{in} (p_{out}). As a consequence, the true flow rate is smaller than that of the flow driven by the constant pressure gradient $(p_{in} - p_{out})/L_0$ in a sufficiently long channel. This effect can be quantified by the length increment ΔL_0 to the total channel length [33]. Then, the Darcy law (1) should be modified to

$$G_p = -\frac{\sqrt{\pi}}{2Kn}\frac{k_a}{(L_0 + 2\Delta L_0)/H}\Delta p, \tag{12}$$

where k_a is the AGP of the infinite long channel and $\Delta p = (p_{out} - p_{in})/\bar{p}$ is the gas pressure difference between the outlet and inlet reservoirs normalized by the average gas pressure. Note that the relation (12) is presented in a dimensionless form with $G_p = \overline{U}/v_m$, i.e., the dimensionless mass flow rate (7) is equal to the discharge per time normalized by the most probable speed v_m of gas molecules. Again, we consider the representative case of $Kn = 10$.

4.1 Numerical settings

To determine the pressure jump and incremental length for flows in angstrom-scale channels under gas-surface interactions with different values of accommodation coefficient, we choose four accommodation coefficients $\alpha = 1, 10^{-1}, 10^{-2}, 10^{-4}$. A small pressure difference is imposed, i.e., $(p_{in} - p_{out}) \ll p_{in}$; thus, the pressure jumps (or the length increments) at the inlet and outlet cross sections are identical. To demonstrate the length dependence of the flow rate, we consider the channel length in the range of $L_0/H \in [5, 5000]$. The dimension of simulation domain for each reservoir is $L_1 \times H_1$ with $H_1 = H/2 + L_1$. As shown in Fig. 9, the boundaries labeled by 'ⓦ' are solid surfaces, with the boundary condition given in Eq (5); these labeled by 'ⓟ' are pressure inlet/outlet boundaries, where the boundary condition is specified as

$$
\begin{cases}
f(\boldsymbol{x}, \boldsymbol{v}) = (p_{in} - \bar{p})/\bar{p}, & \text{for } \boldsymbol{v} \cdot \boldsymbol{n} \geq 0 \text{ at inlet}, \\
f(\boldsymbol{x}, \boldsymbol{v}) = (p_{out} - \bar{p})/\bar{p}, & \text{for } \boldsymbol{v} \cdot \boldsymbol{n} < 0 \text{ at outlet};
\end{cases}
\tag{13}
$$

and the horizontal center line labeled by 'ⓢ' is a symmetry boundary: $f(\boldsymbol{x}, v_1, v_2) = f(\boldsymbol{x}, v_1, -v_2)$. Macroscopic flow properties of interest are gas pressure and flow velocity. In an isothermal case, the gas pressure is related to the number density n (calculated according to Eq. (4)) through $\frac{p}{\bar{p}} - 1 = n$.

The discontinuous Galerkin method is employed to discretize the kinetic Eq. (3) in the spatial space, where the computational domain is partitioned by regular disjoint triangles. In order to obtain grid-independent results, we run the simulation on meshes with different triangle sizes to ensure that a further mesh refinement does not change the pressure and velocity fields with magnitudes larger than 0.5%. We also repeat the simulation to determine the size of L_1 and make sure the results are independent of the reservoir size. Eventually, $L_1/H = 50$ is chosen for all considered cases. Non-uniform meshes with refinement near the solid surfaces are used, where the cell sizes (the height of a triangle, h_Δ) vary in $0.1 \leq h_\Delta/H \leq 7$. The other computational parameters are the same as those used in the previous section. Note that the flow is essentially multiscale, so the general synthetic iterative scheme is used here to boost the convergence in numerical simulations; numerical details can be found in Refs. [30, 36].

4.2 Mass flow rate

The dimensionless mass flow rate G_p divided by $-\Delta p$ as functions of the channel length is illustrated in Fig. 10 for different values of accommodation coefficient. It is found that the mass flow rate has relatively small values when the fully diffuse gas-surface interaction is enforced. Besides, it scales down approximately by a factor of $1/L_0$ when the channel length increases. Driven by the same pressure difference, the mass flow rate is largely enhanced when the accommodation coefficient is decreased. When $\alpha = 10^{-4}$, the mass flow rate remains constant when the channel length varies within the considered range. Consequently, the mass flow rate of $\alpha = 10^{-4}$ can be three orders of magnitude larger than that of $\alpha = 1$ in a relatively long channel (e.g., $L_0/H = 5000$). The mass flow rates with $\alpha = 0.1$ and 0.01 also decrease with increasing channel length, but it is much slower than the scaling of $1/L_0$ under the case of fully diffuse scattering.
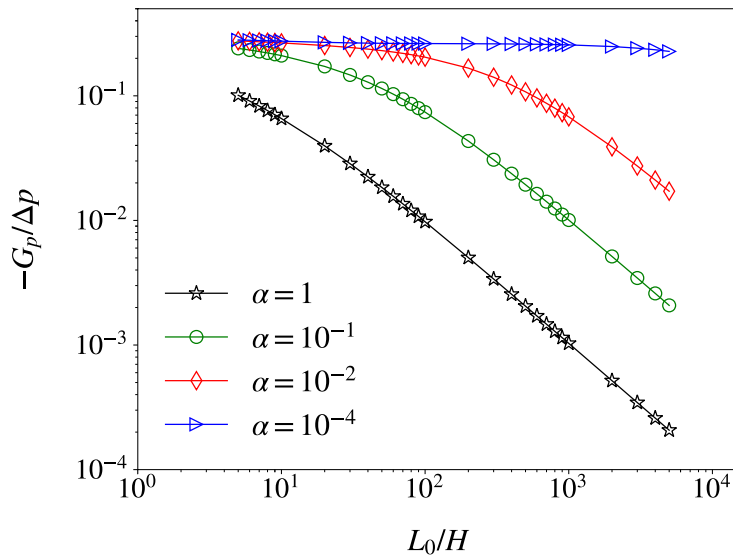
Fig. 10 Dimensionless mass flow rate in a channel with finite length

4.3 End correction length

In order to understand how the inlet and outlet ends of the channel affect the gas flow, we plot the gas pressure distribution along the horizontal center line of the channel connecting to two gas reservoirs in Fig. 11. The channel length is $L_0/H = 100$. It is shown that the pressure changes nearly with a constant gradient m_α in the central region of the channel. That is, the pressure inside the channel, say, $0.3L_0/H \leq x_1 \leq 0.7L_0/H$, can be fitted as

$$\frac{p - p_{\text{out}}}{p_{\text{in}} - p_{\text{out}}} = m_\alpha \left(x_1 - \frac{L_0}{2H} \right) + \frac{1}{2}. \tag{14}$$
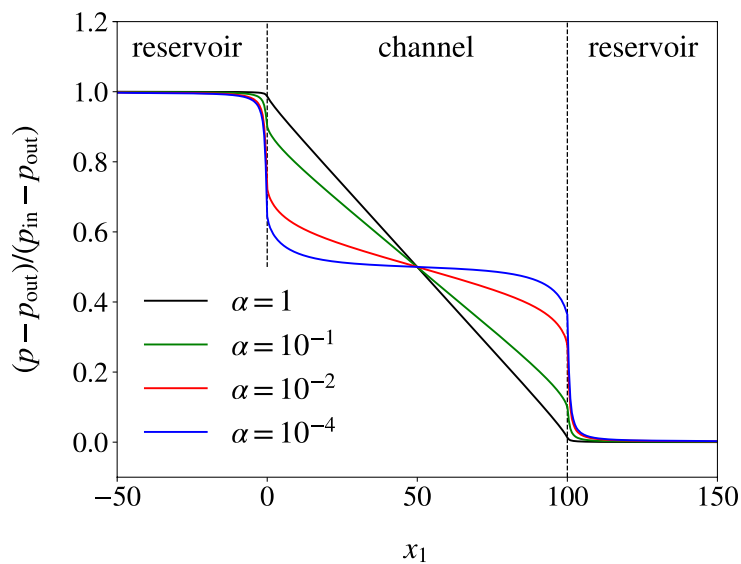

Fig. 11 Normalized pressure distribution along the horizontal center line of a channel connecting to two gas reservoirs. The channel length is $L_0/H = 100$

The absolute value of the gradient m_α decreases with the accommodation coefficient; consequently, for a given length L_0, the channel with a smaller accommodation coefficient suffers larger end effect, where the gas pressure varies significantly in the vicinity of the inlet and outlet. These trends hold for channels with other lengths.

To quantify the end effect, we calculate the length increment ΔL_0; the larger the length increment, the more significant the end effect will be. As shown in Fig. 9, it is defined as the distance between the inlet (outlet) cross section and the position at which the pressure reaches p_{in} (p_{out}) according to the linear extrapolation of the pressure curve inside the channel; from some algebraic calculations, we have

$$\frac{\Delta L_0}{H} = -\frac{1}{2m_\alpha} - \frac{L_0}{2H}. \tag{15}$$

The increments ΔL_0 for selected channel lengths and different accommodation coefficients are listed in Table 1. It is shown that for a fixed channel length, ΔL_0 increases with decreasing accommodation coefficient.

Figure 10 shows that the mass flow rate scales down with the channel length by a factor of $1/L_0$ under fully diffuse gas-surface scattering, but remains constant when the accommodation coefficient is rather small. This can be explained by the end correction length. The dimensionless mass flow rate can be estimated by the Darcy law (12) when the channel length is relatively long, say, $L_0/H \geq 500$. Note that for a channel without small bumps, the gas permeability k_a is independent of L_0, although its values are different for different accommodation coefficients. Therefore, for a given α, we have

Table 1 End effect for channel with finite length: the length increment ΔL_0 obtained from Eqs. (14) and (15)

$\frac{L_0}{H}$	α	$\frac{\Delta L_0}{H}$	$\frac{1}{(L_0+2\Delta L_0)/H}$	$\frac{L_0}{H}$	α	$\frac{\Delta L_0}{H}$	$\frac{1}{(L_0+2\Delta L_0)/H}$
5	1	1.258×10^0	1.331×10^{-1}	200	1	3.136×10^0	4.848×10^{-3}
	10^{-1}	7.020×10^0	5.252×10^{-2}		10^{-1}	2.056×10^1	4.147×10^{-3}
	10^{-2}	1.359×10^1	3.107×10^{-2}		10^{-2}	1.700×10^2	1.852×10^{-3}
	10^{-4}	1.533×10^1	2.805×10^{-2}		10^{-4}	7.401×10^3	6.666×10^{-5}
10	1	1.595×10^0	7.581×10^{-2}	500	1	4.801×10^0	1.962×10^{-3}
	10^{-1}	9.731×10^0	3.394×10^{-2}		10^{-1}	1.910×10^1	1.858×10^{-3}
	10^{-2}	2.268×10^1	1.806×10^{-2}		10^{-2}	1.729×10^2	1.182×10^{-3}
	10^{-4}	2.695×10^1	1.565×10^{-2}		10^{-4}	1.674×10^4	2.944×10^{-5}
20	1	2.051×10^0	4.149×10^{-2}	1000	1	5.530×10^0	9.891×10^{-4}
	10^{-1}	1.325×10^1	2.151×10^{-2}		10^{-1}	9.757×10^0	9.809×10^{-4}
	10^{-2}	4.219×10^1	9.580×10^{-3}		10^{-2}	1.724×10^2	7.436×10^{-4}
	10^{-4}	5.798×10^1	7.355×10^{-3}		10^{-4}	1.647×10^4	2.947×10^{-5}
50	1	2.698×10^0	1.805×10^{-2}	2000	1	5.656×10^0	4.972×10^{-4}
	10^{-1}	1.788×10^1	1.166×10^{-2}		10^{-1}	6.036×10^0	4.970×10^{-4}
	10^{-2}	9.926×10^1	4.024×10^{-3}		10^{-2}	1.604×10^2	4.309×10^{-4}
	10^{-4}	2.484×10^2	1.829×10^{-3}		10^{-4}	1.524×10^4	3.079×10^{-5}
100	1	2.911×10^0	9.450×10^{-3}	5000	1	5.676×10^0	1.995×10^{-4}
	10^{-1}	1.997×10^1	7.146×10^{-3}		10^{-1}	6.932×10^0	1.994×10^{-4}
	10^{-2}	1.497×10^2	2.504×10^{-3}		10^{-2}	3.054×10^1	1.976×10^{-4}
	10^{-4}	1.191×10^3	4.028×10^{-4}		10^{-4}	1.471×10^4	2.905×10^{-5}

$$-\frac{G_p}{\Delta p} \propto \frac{1}{(L_0 + 2\Delta L_0)/H}. \tag{16}$$

The quantities $1/[(L_0 + 2\Delta L_0)/H]$ are listed in the fourth column of Table 1, which can be approximated as

$$\frac{1}{(L_0 + 2\Delta L_0)/H} \simeq \begin{cases} 0.98\frac{H}{L_0}, & \text{for } \alpha = 1, \\ 2.9 \times 10^{-5}, & \text{for } \alpha = 10^{-4}, \end{cases} \tag{17}$$

when $500 \leq L_0/H \leq 5000$. Therefore, when the accommodation coefficient is sufficiently small, the end effect is so intensive that the mass flow rate is independent of the channel length.

4.4 Flow enhancement

With the data in the previous sections, we visualize the flow enhancement coefficient K (i.e., the ratio of the measured flow rate to the value calculated by the Knudsen theory) in Fig. 12. It is found that, when the accommodation coefficient is fixed, as the channel length increases, the enhancement coefficient first increases with the channel length linearly, and then saturates to a value which is roughly given by Eq. (11). When the effective accommodation coefficient is small, the linear increase of enhancement with the channel length is also observed in Ref. [19], see Fig. 3b therein. Also, when the channel length is fixed, but the channel height increases, the enhancement coefficient decreases because L_0/H decreases, which is consistent with the molecular dynamic simulation in Ref. [19], see Fig. 3b therein. This comparison demonstrates the reliability of our kinetic treatment of the gas flow problem.
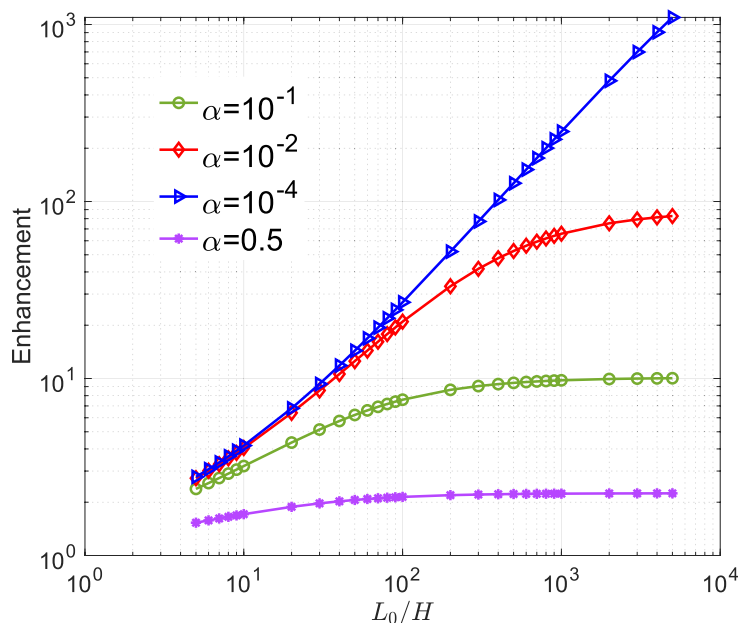

Fig. 12 Enhancement (i.e., the mass flow rate normalized by that of the finite-length channel with the diffuse scattering) of the mass flow rate as a function of the channel length

5 Explanation of experiment

Based on the numerical findings in the previous two sections, we are now in the position to explain the experimental phenomenon reported in Ref. [13]. First, it is found that the permeability in graphite and hBN devices is not a function of the channel length L_0, while the permeability in MoS_2 channel scales down as $1/L_0$, see Fig. 2b in Ref. [13]. Since in the experiment the ratio between channel length and height is about 10^3 (i.e., the channel height is about 1.36 nm, while the length varies from 1 to 15 μm), from Fig. 10 it can be inferred that the graphite and hBN devices have an effective accommodation coefficient of $10^{-3} \sim 10^{-4}$ (i.e., gas molecules undergo near-specular scattering at the channel surface), while the MoS_2 channel has an effective accommodation coefficient $\alpha \sim 1$ (i.e., gas molecules undergo diffuse scattering at the channel surface). Were the graphite and hBN devices made longer, the mass flow rate would begin to decrease.

Second, it is found in the experiment that "within the data scatter, the gas flow through MoS_2 channels is described well by the Knudsen theory of diffuse scattering, while all graphite and hBN devices exhibited strong enhancement reaching $K > 100$". For the latter devices, when the channel height is small, K increases with the channel height [13]. This can be understood as follows. When the height increases, the ratio between the channel height and the bump height increases, so that according to Eq. (10) the effective accommodation coefficient decreases, and the enhancement ratio increases. In the experiment, $K \approx 100$, then according to the data in Fig. 12 the effective accommodation coefficient is about 10^{-2}. Therefore, as per Eqs. (10) and (11), the bump height to the channel height is about 10^{-3}, when w/H is small; while when $w/H \to 1$, the bump height to the channel height is about 10^{-2} (this can be deducted from Fig. 8). Both cases indicate an atomically-flat surface.

We notice that, at each channel height, the experimentally measured enhancement has large error bars, for instance, when $H = 1.36$ nm, K varies from 80 to 300 [13]. Since for the same channel height the channel length in experiment varies significantly, according to Fig. 12 we know the enhancement also has a significant variation when $\alpha_{\text{effective}} \leq 0.01$. This can be used to explain the experimental results with large data scatterings.

On the other hand, when the channel height is large, however, K decreases when the channel height increases, and eventually the enhancement is reduced to 1. This is because the PMMA polymer molecule tends to be absorbed on the graphene surface (see Fig. 2d in Ref. [13]), which forms "bumps" on the channel impeding the gas flow, and the larger the channel height, the easier and higher the bumps are formed.

Third, in the experiment [13], the mass flow rates of deuterium and hydrogen are measured and compared. It is found that the graphene channel with a height of 13.6 nm exhibited permeability $\approx (30 \pm 10)\%$ smaller for deuterium than hydrogen. Since both isotopes have the same interaction with the graphene but have different de Broglie wavelengths, they drew the conclusion that "this fact unequivocally proves that matter-wave effects contribute to the specular reflection leading to its suppression for heavier atoms because deuterium has a shorter de Broglie wavelength and sees an atomic landscape somewhat rougher than hydrogen". Since the present work only relies on the empirical parameters in Maxwell's diffuse-specular boundary condition,

this phenomenon should be explained based on the density functional theory, molecular dynamic simulation [37, 38], or advanced kinetic models for the gas-surface interaction such as the Enskog-Vlasov collision operator [39, 40] and the Boltzmann-type gas-phonon collision operator [41]. Here we point out one possible fact that, at the same temperature, the mean thermal speed of deuterium is smaller than hydrogen, and in the Epstein kinetic boundary condition [25, 42] or molecular dynamic simulations [43, 44], it can be found that larger speed molecules are less likely trapped by the wall molecules and hence a smaller effective accommodation coefficient. In other words, even without involving the quantum effect, the smaller mass flow rate of deuterium than hydrogen can be explained in terms of the relative large accommodation coefficient. This will be subject to our future work.

6 Conclusions

In summary, we have investigated the behavior of a two-dimensional pressure-driven gas flow through a finite-length channel with rough elements in the form of rectangular bumps. The apparent gas permeability in the rough channel is obtained by solving the gas kinetic equation under Maxwell's diffuse-specular gas-surface boundary condition. Our results have shown that the properties of gas flow in rough channels are the combined result of multiple factors such as the tangential momentum accommodation coefficient (α), the size of bumps, and the channel length. The main findings could be summarized as follows:

1. In the rough channel with small values of accommodation coefficient, the pressure-driven flow could exhibit an inverted streamwise velocity profile, that is, the flow velocity near the solid surface could be larger than that in the middle of the channel, see Fig. 4.

2. In the rough channel, even if the size of bumps is very small, the small disturbance caused by it can penetrate into the main flow area and affect the flow characteristic of the whole channel. Specifically, in the free-molecular regime, when the accommodation coefficient is very small, the apparent gas permeability will be dramatically reduced by the presence of bumps, to a value that is almost comparable to that of the accommodation coefficient ≈ 0.5, see Fig. 7.

3. In the free-molecular regime, the end effect is rather significant when the effective accommodation coefficient of the channel is very small, such that the mass flow rate will be much reduced when the channel is not long enough, see Fig. 10. Based on the numerical simulations, we have tabulated the end correction length at typical values of accommodation coefficient and channel length in Table 1, which will be useful for engineering corrections.

Based on the numerical simulations, we have properly explained the exotic mass flow rate in hBN and graphene channels, as observed in the experiment [13] and molecular dynamic simulation [19].

Although here we only consider the linearized flow, we believe the role of bumps in increasing the effective tangential momentum accommodation coefficient also occurs in high-speed, highly rarefied gas flows, e.g., space stations and vehicles flying at upper-atmosphere with high speeds.

Availability of data and materials
The data that support the findings of this study are available from the corresponding author upon reasonable request.

Declarations

Competing interests
The authors declare that they have no competing interests.

References

1. Javadpour F, Fisher D, Unsworth M (2007) Nanoscale gas flow in shale gas sediments. J Can Pet Technol 46(10):55–61
2. Sholl D, Lively R (2016) Seven chemical separations to change the world. Nature 532:435–437
3. Zhang LH, Shan BC, Zhao YL et al (2019) Review of micro seepage mechanisms in shale gas reservoirs. Int J Heat Mass Transf 139:144–179
4. Loucks RG, Reed RM, Ruppel SC et al (2009) Morphology, genesis, and distribution of nanometer-scale pores in siliceous mudstones of the Mississippian Barnett Shale. J Sediment Res 79(12):848–861
5. Yan GY, Wei CT, Song Y et al (2018) Quantitative description of shale pore structure using image analysis and determination of controls on shape, size and orientation complexity. Arab J Geosci 11:11
6. Curtis ME, Sondergeld CH, Ambrose RJ et al (2012) Microstructural investigation of gas shales in two and three dimensions using nanometer-scale resolution imaging. AAPG Bull 96(4):665–677
7. Javadpour F (2009) Nanopores and apparent permeability of gas flow in mudrocks (shales and siltstone). J Can Pet Technol 48(08):16–21
8. Darabi H, Ettehad A, Javadpour F et al (2012) Gas flow in ultra-tight shale strata. J Fluid Mech 710:641–658
9. Beskok A, Karniadakis GE (1999) Report: a model for flows in channels, pipes, and ducts at micro and nano scales. Microscale Thermophys Eng 3(1):43–77
10. Civan F (2010) Effective correlation of apparent gas permeability in tight porous media. Transp Porous Med 82(2):375–384
11. Klinkenberg LJ (1941) The permeability of porous media to liquids and gases. Drilling and production practice. American Petroleum Institute, Washington DC, pp 200–213
12. Holt JK, Park HG, Wang Y et al (2006) Fast mass transport through sub-2-nanometer carbon nanotubes. Science 312(5776):1034–1037
13. Keerthi A, Geim AK, Janardanan A et al (2018) Ballistic molecular transport through two-dimensional channels. Nature 558(7710):420–424
14. Wang L, Boutilier MSH, Kidambi PR et al (2017) Fundamental transport mechanisms, fabrication and potential applications of nanoporous atomically thin membranes. Nature Nanotech 12:509–522
15. Steckelmacher W (1966) A review of the molecular flow conductance for systems of tubes and components and the measurement of pumping speed. Vacuum 16(11):561–584
16. Wu L, Ho MT, Germanou L et al (2017) On the apparent permeability of porous media in rarefied gas flows. J Fluid Mech 822:398–417
17. Majumder M, Chopra N, Hinds BJ (2011) Mass transport through carbon nanotube membranes in three different regimes: Ionic diffusion and gas and liquid flow. ACS Nano 5(5):3867–3877
18. Bhatnagar PL, Gross EP, Krook M (1954) A model for collision processes in gases. I. small amplitude processes in charged and neutral one-component systems. Phys Rev 94:511–525
19. Qian JH, Li YH, Wu HA et al (2021) Surface morphological effects on gas transport through nanochannels with atomically smooth walls. Carbon 180:85–91
20. Mo G, Rosenberger F (1990) Molecular-dynamics simulation of flow in a two-dimensional channel with atomically rough walls. Phys Rev A 42:4688–4692
21. Kamali R, Kharazmi A (2011) Molecular dynamics simulation of surface roughness effects on nanoscale flows. Int J Therm Sci 50(3):226–232
22. Cao BY, Chen M, Guo ZY (2006) Effect of surface roughness on gas flow in microchannels by molecular dynamics simulation. Int J Eng Sci 44(13–14):927–937
23. Sharipov F, Fahrenbach P, Zipp A (2005) Numerical modeling of Holweck pump. J Vac Sci Technol A 23:1331–1339
24. Pham-Van-Diep G, Erwin D, Muntz EP (1989) Nonequilibrium molecular motion in a hypersonic shock wave. Science 245:624–626
25. Wu L, Struchtrup H (2017) Assessment and development of the gas kinetic boundary condition for the Boltzmann equation. J Fluid Mech 823:511–537

26. Maxwell JC (1879) On stresses in rarefied gases arising from inequalities of temperature. Philos Trans R Soc Lond 170:231–256
27. Su W, Lindsay S, Liu HH et al (2017) Comparative study of the discrete velocity and lattice Boltzmann methods for rarefied gas flows through irregular channels. Phys Rev E 96(2):023309
28. Takata S, Funagane H (2011) Poiseuille and thermal transpiration flows of a highly rarefied gas: over-concentration in the velocity distribution function. J Fluid Mech 669:242–259
29. Wu L, Reese JM, Zhang YH (2014) Solving the Boltzmann equation deterministically by the fast spectral method: application to microflows. J Fluid Mech 746:53–84
30. Su W, Ho MT, Zhang YH et al (2020) GSIS: an efficient and accurate numerical method to obtain the apparent gas permeability of porous media. Comput Fluids 206:104576
31. Su W, Zhu LH, Wang P et al (2020) Can we find steady-state solutions to multiscale rarefied gas flows within dozens of iterations? J Comput Phys 407:109245
32. Pantazis S, Valougeorgis D, Sharipov F (2013) End corrections for rarefied gas flows through capillaries of finite length. Vacuum 97:26–29
33. Pantazis S, Valougeorgis D, Sharipov F (2014) End corrections for rarefied gas flows through circular tubes of finite length. Vacuum 101:306–312
34. Sharipov F, Seleznev V (1998) Data on internal rarefied gas flows. J Phys Chem Ref Data 27:657–706
35. Kammara KK, Kumar R, Singh AK et al (2019) Systematic direct simulation Monte Carlo approach to characterize the effects of surface roughness on accommodation coefficients. Phys Rev Fluids 4:123401
36. Su W, Zhu LH, Wu L (2020) Fast convergence and asymptotic preserving of the general synthetic iterative scheme. SIAM J Sci Comput 42:B1517–B1540
37. Barisik M, Beskok A (2014) Scale effects in gas nano flows. Phys Fluids 26:052003
38. Barisik M, Beskok A (2016) "Law of the nano-wall" in nano-channel gas flows. Microfluid Nanofluid 20:46
39. Frezzotti A, Gibelli L (2008) A kinetic model for fluid–wall interaction. Proc Inst Mech Eng C J Mech Eng Sci 222:787–795
40. Barbante P, Frezzotti A, Gibelli L (2015) A kinetic theory description of liquid menisci at the microscale. Kinet Relat Models 8:235–254
41. Brull S, Charrier P, Mieussens L (2016) Nanoscale roughness effect on Maxwell-like boundary conditions for the Boltzmann equation. Phys Fluids 28:082004
42. Epstein M (1967) A model of the wall boundary condition in kinetic theory. AIAA J 5:1797–1800
43. Lim WW, Suaning GJ, McKenzie DR (2016) A simulation of gas flow: The dependence of the tangential momentum accommodation coefficient on molecular mass. Phys Fluids 28:097101
44. Yamaguchi H, Matsuda Y, Niimi T (2017) Molecular-dynamics study on characteristics of energy and tangential momentum accommodation coefficients. Phys Rev E 96:013116

Publisher's Note